A full-field approach for precipitation in metallic alloys. Comparison with a mean-field model

Mathilde Eymann, Michel Perez, Thibaut Chaise, Thomas Elguedj, Pierre-Antoine Geslin

A full-field approach for precipitation in metallic alloys. Comparison with a mean-field model.

Mathilde Eymann[a], Michel Perez[a], Thibaut Chaise[b], Thomas Elguedj[b], Pierre-Antoine Geslin[a,*]

[a] *INSA Lyon, CNRS, Universite Claude Bernard Lyon 1, MATEIS, UMR5510, 69621 Villeurbanne, France*
[b] *INSA Lyon, CNRS, LaMCoS, UMR5259, 69621 Villeurbanne, France*

Abstract

Modelling precipitation in metallic alloys is a topic of great importance in physical metallurgy as the resulting strengthening strongly depends on the precipitate microstructure. We propose here a numerical full-field model for precipitation that describes precipitates with shape functions, thereby allowing to bridge scales between phase-field approaches - that accurately describe the precipitate evolution but require a fine discretization grid - and mean-field approaches - that are computationally very efficient but rely on strong assumptions. Our results demonstrate the capability of the full-field approach to model the different stages of precipitation during isothermal treatments. The comparison with mean-field results allow to discuss the influence of solutal impingement and precipitate coagulations on the evolution of the precipitate microstructure.

Keywords: Modelling, Precipitation, Kampmann-Wagner Numerical (KWN) modelling, Full field modelling

1. Introduction

In precipitate-hardened alloys (e.g. aluminum alloys of the 6000 and 7000 series, and Ni-based super-alloys), thermal treatments allow for the control of the precipitation of secondary phases in order to achieve optimal mechanical properties [1, 2]. First, annealing above the solubility limit allows for the homogeneous dispersion of solute atoms in the alloys. Second, a precipitation treatment at a lower temperature triggers the nucleation and growth of second phase precipitates.

In these alloys, the precipitates form obstacles to dislocation motion and the resulting hardening strongly depends on the size, volume fraction and microstructure of the precipitates [3, 4]. The technological relevance of these alloys as structural materials promoted the development of quantitative modeling tools predicting the evolution of the microstructure. In particular, the precipitate evolution is usually described through three distinct stages: the first stage consists in the nucleation of precipitates from the solid solution; then, the precipitates growth is enabled by the solute diffusion in the surrounding supersaturated medium. Finally, when the solute concentration in the matrix becomes comparable to the equilibrium composition, the system enters a coarsening stage where the Gibbs-Thomson effect promotes the growth of large precipitates and the shrinkage of small ones.

The first major theoretical step on the study of precipitate evolution was performed by Lifshitz, Slyozov and Wagner (LSW) [5, 6] who derived an analytical solution describing the steady-state behavior of interacting precipitates during the coarsening stage. They assume each precipitate to be isolated in an infinite medium. Solving the steady-state diffusion field around a precipitate yields its growth rate as function of its radius. Combining the growth rates for all precipitate sizes allows deriving the size distribution in the steady-state coarsening regime and the coarsening law for the average precipitate radius.

The main limitations of this analytical treatment are (i) the mean-field nature of the theory and the assumption of isolated precipitates, which make the treatment valid only in the limit of vanishing precipitate volume fractions; (ii) the fact that the LSW solution describes the steady-state coarsening stage and does not provide information about the nucleation and growth stages.

Several strategies have been employed to generalize the LSW solution beyond the assumption of vanishing precipitate volume fraction [7]. An elegant solution was

*Corresponding author.
Email address: pierre-antoine.geslin@insa-lyon.fr (Pierre-Antoine Geslin)

proposed by Wang *et al.* [8] and consists in accounting for solutal impingement between precipitates by incorporating a screening length into the diffusion of solutes around isolated precipitates. In the steady-state coarsening regime, the results of this screening diffusion theory were successfully compared to numerical models [8] and experimental results in the case of Al-Li alloys [8, 9].

Modeling the precipitation process in the nucleation and growth stages also seems desirable to simulate microstructure evolution at the beginning of the precipitation treatments. Kampmann and Wagner introduced a numerical model (also known as KWN model) combining the classical nucleation theory with a mean-field treatment of precipitate growth and coarsening [10]. As in the LSW theory, each precipitate is assumed to interact with an average medium. Easy to implement and relatively fast in execution, KWN-type models are now widespread: they are implemented either in "Euler-like" approach (solving fluxes between neighbouring size classes), or in "Lagrange-like" approach (solving time evolution of precipitate size classes) [11]. They can be found in the form of open software (*e.g.* "PreciSo" [11], Kawin [12]) or more accomplished commercial packages (*e.g.* "Mathcalc" [13, 14, 15], "TC-Prisma" [16]). Beyond homogeneous isothermal thermal treatments, processing techniques such as additive manufacturing and welding lead to rapid, heterogeneous thermal history that greatly affect the precipitation microstructure. Adapting these modelling tools to this type of heat treatment is a challenging ongoing task [17, 18, 19].

In recent formulations of the KWN models, the growth rate of precipitates is modified to account for precipitate interactions through solutal impingement [20, 21, 22]. This type of technique will be referred to as mean-field approaches in the following and will be used as a benchmark to compare results obtained from our full-field model. More details about these approach and their numerical integration are given in Appendix A.

These numerical approaches, despite their versatility, rely on a mean-field description and can only account for solutal impingement in an approximated manner [8, 20, 21, 22]. In addition, they do not provide information on the positions of precipitates in space nor on their spatial correlations. Full-field approaches overcome such limitations by modeling the microstructure as a set of precipitates located at different positions in the simulated volume. Voorhees and Glicksman proposed a multi-particle diffusion model [23] to investigate the coarsening of an ensemble of particles described with a spherical shape function and interacting through their stationary diffusion field. This numerical model remains however limited to describing the coarsening stage and does not include nucleation nor coagulation of precipitates.

Phase-field modeling can be seen as a more comprehensive full-field approach [24, 25]. The precipitate/matrix interfaces are described through the variations of an auxiliary phase field, which facilitate the description of arbitrary precipitate shapes and topological changes due to the coagulation of neighboring precipitates. These approaches are highly versatile and allow to incorporate the role of anisotropic surface energy [26, 27] and elastic interactions [28, 29, 30]. Phase-field models have been used to investigate the evolution of interacting precipitates [31, 32, 30, 33, 34] and to discuss the validity of the mean-field descriptions presented above. However, phase-field methods requires descriptions of interface with a finite width that have to be significantly smaller than the capillary length and the precipitate radius to capture accurately the Gibbs-Thomson effect. Such description requires a discretization on a fine numerical grid, which comes at a numerical cost. Despite a recent formulation mitigating this issue [35], accessible length-scale and time scales remains limited and investigating the evolution of a large number of precipitates is computationally expensive.

In this article, we present a full-field method enabling to describe the nucleation, growth and coarsening of precipitates in a binary alloy, at a mesoscopic scale. To go beyond the length and time-scale limitations of phase-field models, we do not aim at describing the details the precipitate-matrix interface. Instead, the precipitate/matrix interfaces are considered to be sharp and are described with a shape-function. The diffusion equation is solved numerically between precipitates and their growth rate is obtained by integrating the solutal flux on the precipitate surface.

Such mesoscale approach relying on shape functions was used to model dendritic solidification [36, 37]. This formalism allows to simulate large dendritic microstructures out of reach of phase field models while accounting for diverse mechanisms such as the nucleation of new grains [38, 39] or the influence of fluid flow [40, 41]. This meso-scale approach therefore emerged as a scale-bridging tool between physically-based phase-field models and coarse-grained approaches that rely on simplifying assumptions and to discuss the domain of validity of these simplifications [38, 39, 41].

Similarly, the aim of the sharp interface full-field model developed here is to model precipitation within

a representative volume and to compare the results to a mean-field approach for precipitation in order to discuss the assumptions it relies on. We employ material parameters pertaining to Al-Sc alloys. It is considered as a model system to study precipitation kinetics because of the formation of spherical nano-precipitates and the fact that the thermodynamics and kinetics coefficients have been well assessed [42, 43, 44]. The article is organized as follows: the full-field model and its numerical implementation are presented in section 2. Next, the model is validated in section 3 by comparing its results with known analytical solutions and by monitoring solute conservation alongside different mechanisms. Section 4 discusses the model's results and the comparison with mean-field models.

2. Sharp interface full-field model: ShIFuMo

2.1. Physical ingredients

The full-field model named ShIFuMo (Sharp Interface Full-field Model) is based on several ingredients to describe the precipitation state during a heat treatment. The model aims at describing nucleation, growth and coarsening of precipitates denoted p in a matrix denoted m. The system studied here is a binary AB system (A being the solvent and B the solutes) where we assume the formation of stoichiometric precipitates A_xB_y. In this work, precipitates are considered spherical even though other shape functions (e.g. cuboidal, ellipsoidal) can be considered.

We denote X (respectively C) the molar (volume) concentration of solutes B that are related by $X = Cv_m^{at}$, v_m^{at} being the atomic volume of the matrix. We denote X_{eq} the equilibrium concentration given by the phase diagram and X_p the molar composition of solutes in the precipitate: $X_p = y/(x+y)$.

Fig. 1 summarizes the ingredients of the model which are described in the following.

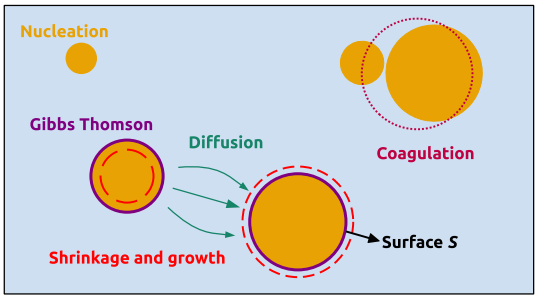

Figure 1: Schematic representation of the ingredients used in the model to describe the precipitation of a second phase.

2.1.1. Classical nucleation theory

The nucleation of new precipitates is described by the classical nucleation theory [19, 5, 6, 11], that is briefly recalled in the following. Let us consider a spherical precipitate germ of radius R. The difference of Gibbs energy of the system brought by this germ is linked to the competition between a positive interfacial energy contribution (proportional to the precipitate/matrix interface) and a negative energy contribution (proportional to the volume of the precipitate):

$$\Delta G = S_p\gamma + V_p\Delta g = 4\pi R^2\gamma + \frac{4}{3}\pi R^3\Delta g, \qquad (1)$$

where γ is the precipitate/matrix interface energy and Δg is the difference of free energy per unit volume between the precipitate and the matrix phases. This quantity depends on the composition: it is nil if the concentration of the matrix matches the equilibrium concentration X_{eq} given by the phase-diagram, and becomes negative for higher concentrations. It is common to express this quantity as follows [19]:

$$\Delta g = -\frac{k_BTy}{(x+y)v_p^{at}}\ln\left[\frac{X_0^x(1-X_0)^y}{X_{eq}^x(1-X_{eq})^y}\right], \qquad (2)$$

where k_B is the Botlzmann constant, T the temperature, v_p^{at} the atomic volume of the precipitate, x and y are the stoichiometric coefficients of the precipitate. This expression is commonly written as a function of the solubility product $K = X_{eq}(T)^x(1-X_{eq}(T))^y$, where $X_{eq}(T)$ is the equilibrium composition given by the phase diagram at temperature T. Furthermore, the dependence of K with temperature can be captured by considering:

$$K(T) = 10^{-\frac{A}{T}+B+\frac{C}{T^2}}, \qquad (3)$$

where A, B, and C are constants. Such expression is chosen because in the limit $X_{eq} \ll X_p$, where the solid solution can be described by an ideal solution model, $A = -\Delta H/k_B$, $B = -\Delta S/k_B$ and $C = 0$. The term C enables to account for higher-order terms emerging away from the limit $X_{eq} \ll X_p$.

In order to become a stable precipitate, a nucleus has to overcome the Gibbs energy barrier described as the maximum of Eq. (1):

$$\Delta G^* = \frac{16}{3}\pi\frac{\gamma^3}{\Delta g^2} \qquad (4)$$

This maximum is reached for a critical radius

$$R^* = -\frac{2\gamma}{\Delta g}. \quad (5)$$

Based on these considerations, the classical nucleation theory describes the nucleation rate as an Arrhenius function of this energy barrier [45]. More precisely, following previous works [46], the nucleation rate per unit time and unit volume is expressed as:

$$\frac{dN}{dt}(X) = N_0 \beta^* Z \exp\left[\frac{-\Delta G^*(X)}{k_B T}\right]\left(1 - e^{-t/\tau}\right) \quad (6)$$

where $N_0 = 1/v_m^{at}$ is the density of nucleation sites, $\beta^* = 4\pi R^{*^2} DX/(a^4 X_p)$ is the condensation rate of monomers on a precipitate of critical radius, a is the lattice parameter, $Z = v_p^{at}(x+y)\sqrt{\gamma/(k_B T)}/(2\pi R^{*2})$ is the Zeldovich's factor and $\tau = 2/(\pi Z^2 \beta^*)$ is the incubation time.

In our full-field approach, the concentration X varies spatially and dN/dt is then also a function of space, such that nucleation events are more probable in regions containing higher concentrations of solutes.

The nuclei of size R^* are as likely to grow as to shrink, both evolutions leading to reduce the system energy. In practice, we consider that nucleating precipitates have a radius [11]:

$$R^*_{kT} = R^* + \frac{1}{2}\sqrt{\frac{k_B T}{\pi\gamma}}. \quad (7)$$

2.1.2. Diffusion and precipitate evolution

Another consequence of the competition between surface and volume energy contributions is the change of equilibrium concentration emerging from the curvature of the precipitate/matrix interface, also referred to as the Gibbs-Thomson effect. For a spherical stoichiometric precipitate of radius R, the equilibrium composition at its curved interface is given by [47]:

$$X_R = X_{eq} \exp\left[\frac{(x+y)}{y}\frac{l_0}{R}\right], \quad (8)$$

where l_0 is the capillary length expressed as

$$l_0 = \frac{2\gamma v_p^{at}}{k_B T}. \quad (9)$$

In a system containing multiple precipitates, Eq. (8) gives the equilibrium concentration on precipitate interfaces and serves as boundary conditions for the diffusion of solutes between them (i.e. in the matrix phase). We assume that the solute field in the matrix follows the time-dependent diffusion equation

$$\frac{\partial X(r,t)}{\partial t} = D\nabla^2 X(r,t), \quad (10)$$

where D is the diffusion coefficient of solutes in the matrix assumed constant in space.

Integrating Eq. (10) with boundary conditions given by Eq. (8) on the precipitates interfaces leads to solute fluxes from high to low concentration regions, resulting in the growth or shrinkage of existing precipitates. The growth rate of precipitates is obtained by integrating the flux of solutes at the precipitate/matrix interface S and applying mass conservation:

$$\begin{aligned}\frac{dR}{dt} &= \frac{D}{4\pi R^2 (C_p - C_R)}\int_S \boldsymbol{\nabla C}\cdot\boldsymbol{dS} \\ &= \frac{D}{4\pi R^2\left(\frac{v_m^{at}}{v_p^{at}}X_p - X_R\right)}\int_S \boldsymbol{\nabla X}\cdot\boldsymbol{dS}. \end{aligned} \quad (11)$$

where the vector $\boldsymbol{dS}$ denotes the interface normal pointing outwards the precipitate. In particular, after their nucleation, the equilibrium concentration at precipitates interfaces is lower than the composition of the surrounding matrix, promoting fluxes of solutes towards the precipitates and triggering their growth through Eq. (11). During this growth stage, the matrix composition decreases until it becomes comparable to the interfacial concentrations given by Eq. (8). In this situation, solutes flow from small precipitates (with higher interfacial concentration) to large ones, which promotes the shrinkage of the former and the growth of the latter, thereby triggering the coarsening of the precipitates population.

2.2. Numerical implementation

We consider a simulated volume V_{tot} that we discretize regularly in cubic voxels of volume Δx^3. The precipitates are described by a shape function (considered spherical in this work), an evolving radius R and a fixed position in the simulated volume [1]. Thanks to this shape-function description of the precipitates, the grid spacing Δx can be chosen independently from the capillary length l_0.

The system evolves through the time evolution of two fields : the concentration field X and a precipitate field denoted Φ. Each voxel i of the simulated volume has a concentration X_i and is either in matrix state ($\Phi_i = 0$) or in precipitate state ($\Phi_i = 1$) if the center of the voxel is

[1] We note that the drift of precipitates center of mass induced by asymmetrical composition fluxes is not taken into account in the current formulation.

inside the shape function of the precipitate (see Fig. 2). This consideration results in a dual description of a precipitate: it is represented in a discrete fashion by an ensemble of voxels on the grid (i.e. orange voxels on Fig. 2) and also by a radius R evolving continuously in time (red circle on Fig. 2). In particular, the volume of the orange voxels is in general different than the volume enclosed in the sphere of radius R, which has an influence on the way mass conservation is enforced, as it will be discussed later.

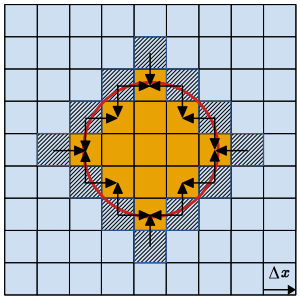

Figure 2: Schematic representation of a precipitate on the discrete numerical lattice. The red circle represents the continuous representation of the precipitate, and the orange voxels depict its discrete representation used to integrate the diffusion equation. The shaded voxels are at the surface of the precipitate where the fluxes (represented with black arrows) are computed to obtain the growth rate.

Nucleation of new precipitates is performed by considering the rate given by Eq. (6) that is composition-dependent and computed on each voxels. The quantity $\frac{dN}{dt}(X_i)\Delta t\Delta x^3$ gives the probability of nucleating a new precipitate on a voxel of volume Δx^3 and composition X_i during the time step Δt. The stochastic character of the nucleation process is reproduced by drawing a random number between 0 and 1 and comparing it to this probability. If the test is passed, a new precipitate of radius $R = R^*_{kT}$ (see Eq. (7)) can be created on the voxel. If it does not overlap with other existing ones, the new precipitate is added. For simplicity, the solute quantity used for this nucleation event is homogeneously subtracted from the matrix of the entire system. This procedure is comparable to what is done in mean-field approaches as the quantity of solute used for nucleation is removed from the matrix composition [10, 11]. Other strategies can be employed, such as the use of a depletion layer that consists in removing solutes locally around the precipitate [48].

The equilibrium concentrations X_R at the precipitates interfaces are computed with Eq. (8) and evolve with the precipitates radius. These concentrations serve as boundary conditions for the diffusion equation and are applied on all the voxels inside the precipitate (orange voxels on Fig. 2).

The diffusion equation (10) is then integrated throughout the matrix by the mean of a simple Euler explicit method of time step Δt. The concentration on each matrix voxel is computed at $t + \Delta t$ from the concentrations on neighboring voxels at time t:

$$X_i^{t+\Delta t} = X_i^t + \frac{D\Delta t}{\Delta x^2}(1 - \Phi_i^t)\left[\sum_n^{neighbors} (X_n^t - X_i^t)\right], \quad (12)$$

where the sum runs over the 6 neighbors of the voxel i. The prefactor $(1 - \Phi_i^t)$ is incorporated to make sure the diffusion occurs only in the matrix and does not affect the concentration in the precipitates.

The growth of a precipitate is obtained from the flux $\mathcal{J}$ of solutes at the precipitate/matrix interface, that is computed as:

$$\mathcal{J} = D \sum_n^{surface} (X_n - X_R)\Delta x \quad (13)$$

where the index n runs on the voxels of the matrix surrounding the precipitates shown in hatched in Fig. 2. The new radius of the precipitate is then computed from the mass balance at the interface:

$$R_{t+\Delta t} = \left[R_t^3 + \frac{3}{4\pi}\frac{\mathcal{J}\Delta t}{\left(\frac{v_m^{at}}{v_p^{at}}X_p - X_R\right)}\right]^{\frac{1}{3}}. \quad (14)$$

A Taylor expansion in the limit $\mathcal{J}\Delta t \ll R_t^3$ can be used to recover a form equivalent to Eq. (11). But for a finite Δt, the integration of this approximated equation leads to the accumulation of small numerical errors that break mass conservation. Therefore, the precipitate radius evolution is computed using Eq. (14).

The evolution of the precipitate radius with time leads to its growth or shrinkage, such that the imprint of the precipitate on the discrete grid (Fig. 2) has to be updated. If a voxel i is initially in the matrix and is captured by a growing precipitate, the solutes it contained is distributed on the neighboring matrix voxels, its concentration is set by the Gibbs-Thomson relation and its state changes to $\Phi_i = 1$. If a voxel belonging to a precipitate is lost because the precipitate shrinks, its concentration does not change and its state shifts to matrix with $\Phi_i = 0$.

When a precipitate becomes very small, the Gibbs Thomson equation diverges, which leads to non-physical behaviors and numerical instabilities. To avoid this divergence, we introduce a threshold radius R_{th}.

This radius is chosen so that the equilibrium concentration at the interface does not exceed the concentration X_p, with a security factor α:

$$R_{th} = \alpha \frac{x+y}{y} l_0 / \ln\left(\frac{X_p}{X_{eq}}\right). \quad (15)$$

In practice, we choose a security factor $\alpha = 1.25$ to remain far from potential numerical instabilities. This choice leads to $R_{th} \simeq 0.3$ nm at the temperature of interest. If $R < R_{th}$, the precipitate is removed from the system, and the solute it contains is homogeneously distributed on the voxels it occupied.

When growing precipitates are close to one another, their interfaces can collide such that their evolution can not be tracked by the integration of Eq. (14). The coagulation of these precipitates is occurring through a transient regime, eventually leading to the formation of a larger spherical precipitate [32]. One of the considerations underlying this meso-scale model is to neglect the complex evolution of the precipitate/matrix interface in this transient regime, such that coagulations are treated as follows. The condition for coagulation is written as:

$$R_i + R_j > d_{ij} + \epsilon, \quad (16)$$

where R_i and R_j are the precipitates radius, d_{ij} is the distance between their centers of mass, and ϵ is a small distance taken as $\epsilon = \Delta x$. If two precipitates meet this condition, they coagulate and they are replaced by a new precipitate. Its position is chosen at the center of mass of both coagulating precipitates and its radius is chosen to conserve mass.

Throughout each step, a special attention is paid to mass conservation in order to avoid any drift of the total solute composition, which will drastically affect the resulting microstructure.

They are multiple ways to compute the total solute content in the system by summing differently the solute content of the matrix and the precipitates. We choose to define the total solute content as:

$$N_{at}^{tot} = \sum_{i=1}^{N_{vox}} X_i \frac{\Delta x^3}{v_m^{at}} + \sum_{n=1}^{N_{ppt}} \frac{4}{3}\pi R_n^3 \left(\frac{X_p}{v_p^{at}} - \frac{X_{R_n}}{v_m^{at}}\right). \quad (17)$$

The first term is the sum on the entire solute content of all the voxels of the system, regardless of their states (matrix of precipitate). Because the composition on the precipitate voxels is fixed, the second term that represents the precipitate contribution includes the difference between X_p and X_{R_n}. Eq. (17) holds the advantage of being consistent with the mass balance embedded in Eq. (14), such that N_{at}^{tot} remains constant upon integration of Eqs. (10) and (14) if the concentration on the precipitate do not evolve in time.

However, when the precipitates grow, their equilibrium composition evolves following the Gibbs-Thomson relation (8), such that both sums of Eq. (17) are modified. In the general case, the discretized volume V_{disc} occupied by the precipitate on the grid that is embedded in the first sum is different than $V_{cont} = 4\pi R^3/3$ used in the second sum. Consequently, changing the value of the precipitate concentration yields a small change in Eq. (17). In order to ensure mass conservation, the corresponding amount of solute is distributed on the matrix surrounding the precipitate:

$$\Delta N_{at} = (V_{disc} - V_{cont})(X_R^{new} - X_R^{prev}), \quad (18)$$

where $(X_R^{new} - X_R^{prev})$ is the composition change of the precipitate attributed to the change of radius through Eq. (8).

This numerical model is implemented using C++/CUDA to harness the computational efficiency of Graphics Processing Units (GPU). The highly parallelized architecture of GPU is especially adapted to the integration of Eq. (12) and to the parallel treatment of precipitates.

In the sharp interface approach proposed here, the grid-spacing Δx is decorrelated from the capillary length and can be chosen of the order of the precipitate size. In practice, we show in Appendix B that the numerical model accurately reproduces the growth of precipitates in a supersaturated matrix if their radius satisfies $R > \Delta x$, while the growth rate obtained for $R < \Delta x$ is impared by significant numerical errors. This is attributed to the numerical description of solute fields around discrete precipitate shapes. As justified in Appendix B, the vast majority of precipitates in our simulations have a radius R¿0 5nm, thereby justifying to consider $\Delta x = 0.5$. Also, the time-step is taken as $\Delta t = 0.1\Delta x^2/D$ to ensure stability of the Euler scheme.

The typical simulated volumes investigated in this article are $128 \times 128 \times 128$ nm^3. The use of modern GPU cards such as the NVIDIA GeForce RTX 3080 Ti, allows to simulate a representative volume over significant time scales thanks to a short computational time of approximately 2×10^{-8} s per unit voxel per time step.

2.3. Materials parameters

We use material parameters pertaining to Al-Sc alloy. In this system, the addition of a small amount of Sc leads to the precipitation of Al_3Sc stoichiometric precipitates.

This system presents the advantage of being experimentally well described [42, 44]. In addition, the nanometric precipitates forming in this alloy are spheroidal, which suits well our model's assumptions.

The parameters used in the simulations are listed in table 1. The values of D_0, Q, and the solubility product coefficients A, B, and C where obtained using the software Thermo-Calc, with the databases TCAL4 and MOBAL3 [49]. A, B, and C were numerically determined by fitting Eq. (3) against the solubility limit obtained from Thermo-Calc.

Material parameters	
matrix atomic vol.	1.6607×10^{-29} m^3
precipitate atomic vol.	1.7293×10^{-29} m^3
solubility product coeffs.	A=2576 K B=0.1158 C=−43 018 K^2
surface energy	0.12 J m^{-2}
D_0	5.3×10^{-4} m^2 s
Q	174 kJ/mol
x	1
y	3

Table 1: Material parameters used in the simulations. The diffusion coefficient is computed as $D = D_0 \exp(-\frac{Q}{RT})$. The solubility product is given by $\log_{10}(K) = -\frac{A}{T} + B + \frac{C}{T^2}$. The lattice parameter is given by $(4v_m^{at})^{1/3}$.

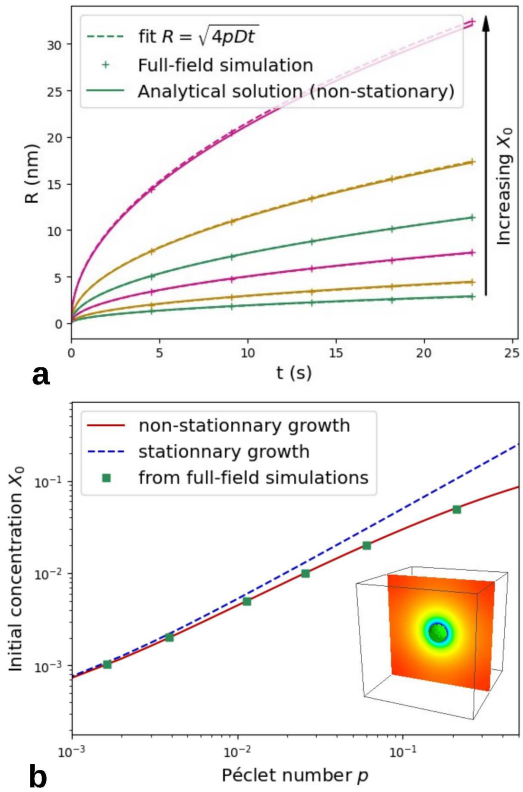

Figure 3: Comparison between model results and the analytical solution for non-stationary growth. (a) shows the evolution of the radius for supersaturation of 0.1, 0.2, 0.5, 1, 2 and 5 at% (bottom to top). (b) shows the relation between the supersaturation and the peclet number, comparing the numerical results with two analytical predictions accounting for stationary and non-stationary growth.

3. Validations

3.1. Model validations

In order to insure that the model implementation is valid, two validation tests are performed. We first check the non-stationary growth of a precipitate in a supersaturated matrix by comparing its growth kinetics to an analytical solution [50]. Second, we monitor the total amount of solutes in four different situations representative of precipitate nucleation, growth, coagulation and disappearance, to check mass conservation in these different situations.

3.1.1. Non-stationary growth

In order to verify the accuracy of the numerical implementation, simulations of the growth of isolated precipitates in supersaturated environments are performed. The simulations are initialized with a precipitate of radius $R = 0.5$ nm, growing in a cubic cell of volume 128^3nm^3. Periodic boundary conditions are employed in all directions. The simulations are performed for different initial matrix concentrations ranging from $X_0 =$ 0.1 at% to $X_0 = 5$ at% and the equilibrium composition at the precipitate/matrix interface is kept at X_{eq} (i.e. the Gibbs-Thomson effect is not considered). Moreover, the atomic volumes of the matrix and the precipitate are here considered equal for simplicity reasons. The growth kinetics of precipitates obtained numerically are shown in Fig. 3.a and are fitted against parabolic laws of the form $\sqrt{4Dpt}$ (dash lines) to deduce the corresponding Péclet number p.

The numerical results are compared to the analytical solution proposed by Zener [50]. This solution is valid for the growth of a spherical precipitate, with an initial radius $R = 0$, growing in a supersaturated infinite matrix with a constant concentration X_{eq} at the precipitate/matrix interface. With these assumptions, the time-integration of the growth equation (11) coupled with the resolution of the time-dependent diffusion equation can be performed analytically and yields a relation between the composition of the supersaturated matrix X_0 and the

Péclet number of the problem defined as $p = \frac{R\dot{R}}{2D}$:

$$\frac{X_0 - X_{eq}}{X_p - X_{eq}} = p^{3/2} e^p \int_p^\infty \frac{e^{-x}}{x^{3/2}} dx. \tag{19}$$

This equation defines a bijective relation between the matrix composition X_0 and the Péclet number p that defines the growth kinetics. This relation is shown with a continuous red line on Fig. 3(b) and allows to compute numerically the Péclet number corresponding to a given matrix composition X_0. Once p is known, integrating $p = \frac{R\dot{R}}{2D}$ gives the growth kinetics of the precipitate:

$$R(t) = \sqrt{4Dpt}. \tag{20}$$

In the limit of small supersaturation, the growth kinetics is slow compared to the equilibration of the solute field, such that the diffusion equation can be considered to be stationary (and is solution of $\nabla^2 X = 0$) along the precipitate growth. This stationary assumption is often considered in the mean-field models for precipitation [10, 11]. With this assumption, the solution of the diffusion problem is straightforward and the precipitate radius growth as:

$$R(t) = \sqrt{2Dt \frac{X_0 - X_{eq}}{X_p - X_{eq}}}, \tag{21}$$

such that the Péclet number associated to this stationary growth is:

$$p = \frac{X_0 - X_{eq}}{2(X_p - X_{eq})}. \tag{22}$$

This relation is shown with a dashed line on Fig. 3(b). As expected, the difference with the non-stationary solution is negligible for small supersaturations and becomes increasingly larger away from this limit. As an example, for a matrix concentration $X_0 = 2\%$, the stationary solution understimates the Péclet number by 34% compared to the non-stationary case.

The precipitate growth rates obtained with the full-field model and reported in Fig. 3 show an excellent agreement with the non-stationary analytical solution. Fig. 3(a) shows the evolution of the radius with time for different concentrations. The results of the simulations are represented with symbols and compared with the analytical solution shown with full lines. For higher matrix concentration, a slight difference appears at the end of the simulation. This is attributed to the finite dimension of the simulation cell and the interactions of solute fields with periodic images.

Fig. 3(b) shows the relation between the initial concentration and the Péclet number obtained from non-stationary and stationary growth solutions. The Péclet

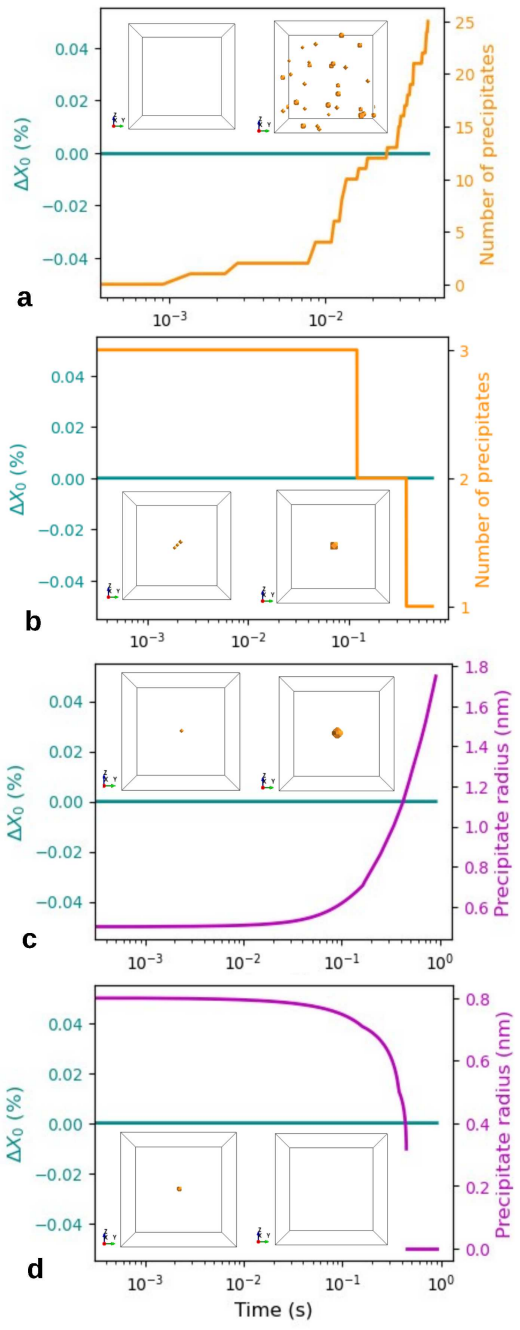

Figure 4: Mass conservation during (a) nucleation, (b) coagulation, (c) growth and (d) shrinkage and disappearance, with snapshots of the simulated system at the beginning and at the end of the simulation. In all cases the horizontal line showing the deviation from the initial concentration in the system highlights the perfect conservation of total solute quantity through the simulation.

number obtained from the fit of the numerical results are reported with symbols and fall on the analytical solution for non-stationary growth. This excellent agreement validates the implementation of precipitate growth and solute diffusion in the numerical model.

3.1.2. Mass conservation

The second validation consisted in monitoring mass conservation along the simulation. As explained above, a special care has been brought to insure that the quantity of solutes in the simulation cell is conserved along the different stages of the simulations: nucleation, growth, coagulation, disappearance. In order to validate mass conservation, simulations have been performed on simple configurations representative of these stages.

The results of the simulations for each case are given in Fig. 4 for four specific cases: (a) nucleation, (b) coagulation, (c) growth and, (d) shrinkage and disappearance of a precipitate. The simulations were performed in a volume $64^3 \mathrm{nm}^3$ with a matrix concentration of 0.8at%, except for case (d), where it was set at 0.05at% to trigger the shrinkage of the precipitate. The snapshots at the start and the end of each simulations are shown. For nucleation (a) and coagulation (b), the evolution of the number of precipitates is given, and for growth (c) and shrinkage (d), the evolution of the radius is shown. In all situations, the total quantity of solutes is perfectly conserved trough the simulation, hence validating each steps of the simulation.

4. Results and comparison with a mean-field model

Full field simulations were performed for different initial concentrations ranging from 1at% to 2.5at%, which correspond to final precipitate volume fractions ranging from $\sim 4\%$ to $\sim 10\%$ approximately.

To better assess the influence of solutal impingement and precipitate coagulation accounted for in the full-field approach, the results are compared with an Eulerian implementation of a mean-field approach taken from Ref. [51] and described in details in Appendix A. This mean-field approach describes the precipitate microstructure with a precipitate size distribution $f(R)$. The ingredients incorporated in this model are similar to the ones used in the full-field formulation: first, the nucleation of precipitates are modeled as described in section 2.1 that gives a nucleation rate of precipitate of size R^*_{kT} as function of the matrix concentration X_m. The growth rate of precipitates of size R is obtained by solving the stationary diffusion equation $\nabla^2 X = 0$ in an infinite medium surronding the precipitate. Each precipitate size R is then associated to a growth rate $v(R)$, which controls the evolution of the precipitate density $f(R)$ during growth and coarsening.

In their original formulations [10], these mean-field models assume that every precipitate interacts with an infinite matrix and therefore neglect the role of solutal impingement on their growth rate. Nevertheless, these formulations can be improved by incorporating the solutal impingement associated to neighbouring precipitates in an approximate manner [20, 21, 22]. A way to account for this effect was proposed by Wang et al. [8] and consists in incorporating a screening length in the growth rate of precipitates. In the following, we refer to this extension of the model as the screened mean-field model. The details of the mean-field models used in this section (with and without incorporating the screening length) are given in Appendix A.

In the following, the evolution of the average radius, the volume fraction and the precipitate density are compared. A special attention is brought to highlight the differences between both mean-field and full-field approaches and to attribute them to the models' assumptions.

4.1. Example of precipitate evolution at $X_0 = 1\%$

At first, simulations are performed with a nominal concentration of $X_0 = 1$ at%. The results are averaged over five independent simulations and are shown in Fig. 5; the snapshots (e-h) show the time evolution of the precipitate microstructure during a simulation. The comparison between the full-field and the mean-field approaches shows a satisfactory agreement. Both models describe the different stages of precipitation as shown in Fig. 5(a) and (c). During the first stage, the nucleation of new precipitates occurs, and they grow by consuming the solute in their vicinity. This growth stage leads to an increase in precipitate size until the average matrix composition becomes comparable to the equilibrium composition given by the Gibbs-Thomson relation. Then a transition from growth to coarsening occurs: the equilibrium composition of small precipitates is larger than for larger ones, thereby triggering composition gradients and solute fluxes from small to large precipitates. Consequently, the large precipitates grow while the small ones shrink and disappear. At this point, the evolution of the precipitate mean radius and density follows a transition plateau. As shown in Fig. 5(c), the precipitates density obtained with both models has a slightly different evolution which will be discussed in section 4.2. In the coarsening regime, larger precipitates continue to grow while smaller ones disappear, leading to an increase of the mean radius and a decrease of the precipitate density. A slight difference between

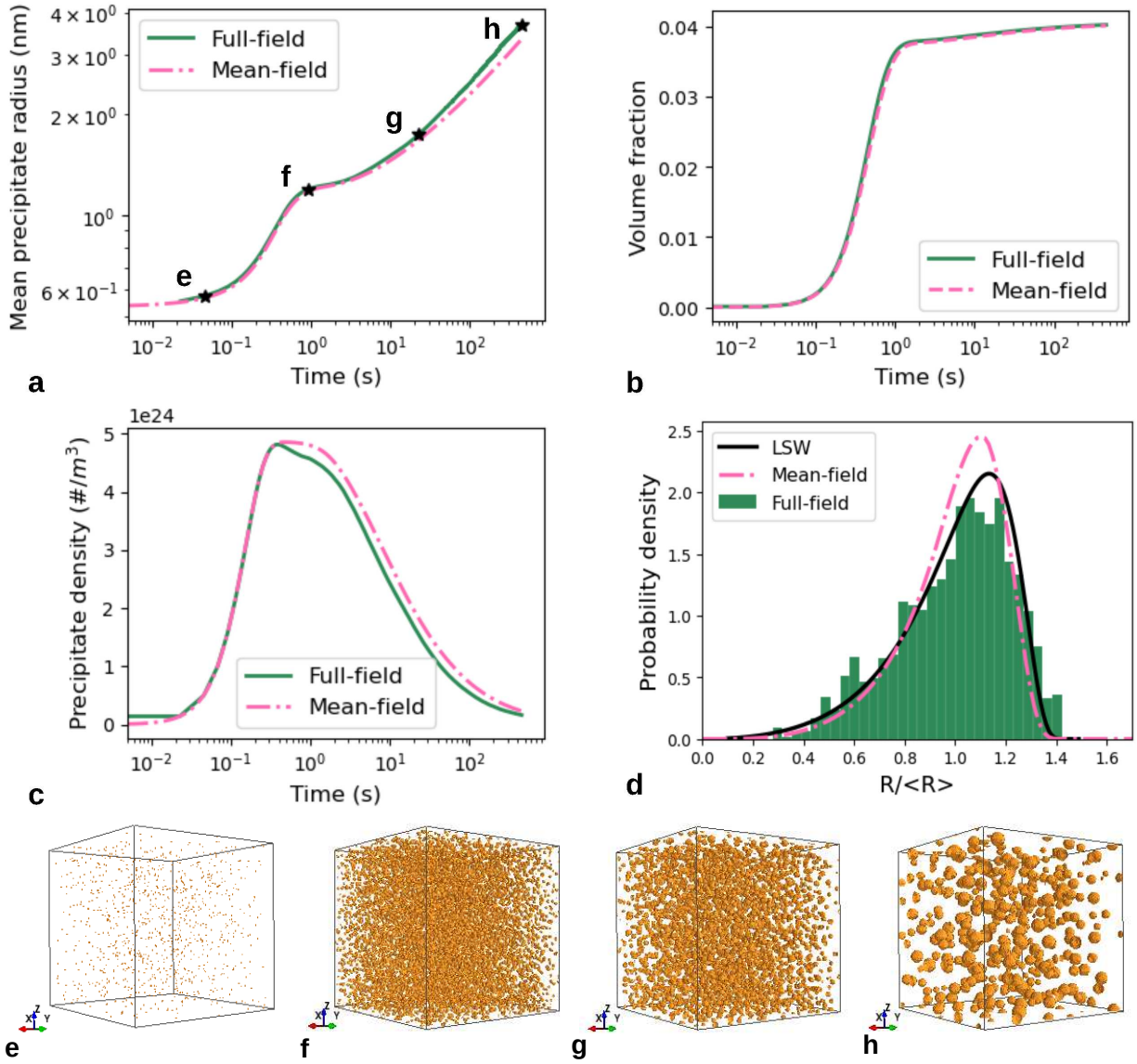

Figure 5: Comparison of the mean-field and full-field model for an alloy concentration $X_0 = 1$ at%. Full-field results are averaged over five independent simulations. Evolutions of (a) the average radius, (b) the volume fraction and (c) the precipitate density, compared with an Eulerian mean-field model. (d) Precipitate size distribution at the end of the simulation, comparison with the LSW theory. (e-h) precipitates microstructures at time $t = 0.045$ s, $t = 0.909$ s, $t = 22.72$ s and $t = 454.3$ s, represented by stars on (a).

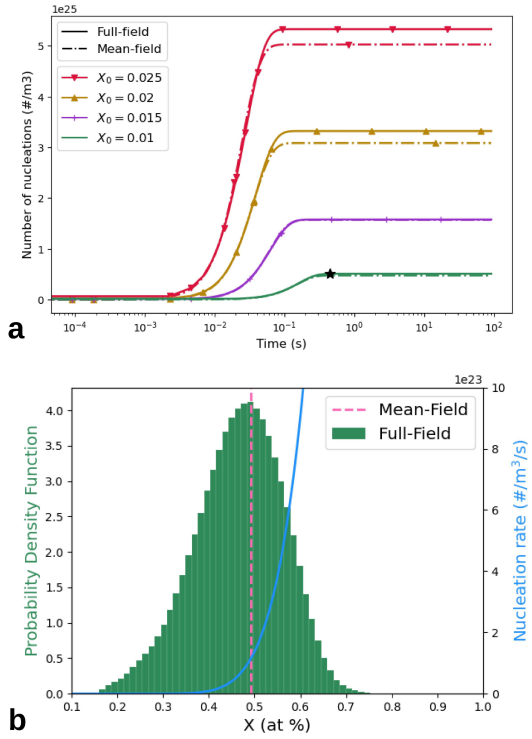

Figure 6: (a) comparisons of the total number of precipitates in full-field and mean-field models. (b) Comparison of the matrix concentrations in mean-field and in full-field for $X_0 = 1$ at.%, with the nucleation rate. The comparison is done at $t = 0.45$ s, indicated with a star on panel (a).

both models appears in the evolution of the mean radius in Fig. 5(a) which will be discussed in section 4.3. Finally, Fig. 5(d) depicts the precipitate density as function of their radius at the end of the simulation (*i.e.* at $t = 454$ s). This probability density can be compared to the prediction of the LSW theory that described the steady-state regime valid at long times. Differences can be seen between the different approaches and will be discussed in section 4.4.

4.2. *Numbers of precipitates: the role of nucleation and coagulations*

As shown on Fig. 5(c), the number of precipitates in the simulated volume varies differently between the full-field and the mean-field model after reaching a peak value at $t \simeq 0.3$ s. These variations are attributed to the coagulation (absent of mean-field models) and nucleation events whose treatment differ slightly in the full-field and mean-field models.

The first mechanism that influences the total number of precipitates is the nucleation stage. Fig. 6(a) shows the number of nucleation events for four initial matrix concentrations for both mean-field and full-field approaches. It shows that there are always more nucleation events in full-field than in mean-field. This can be explained by the composition heterogeneities in the simulated volume emerging from the spatial description of the concentration field in the full-field approach. In contrast, the mean-field approach assumes that nucleation occurs in a matrix of homogeneous composition. This is illustrated in Fig. 6(b) which represents the distribution of the solute concentration in the full-field simulation volume at time $t = 0.45$ s (histogram). The vertical dashed line represents the matrix concentration used in mean-field at the same time. The nucleation rate, shown with a continuous line, evolves exponentially with the solute concentration. While the concentration used in the mean field approach leads to a low nucleation rate, a fraction of the full-field voxels are associated with a high nucleation rate, thereby triggering additional nucleation. The number of nucleation events is therefore higher for the full-field model as shown in Fig. 6(a). This effect is found to be stronger for higher alloy compositions because the composition heterogeneities are more pronounced, leading to a larger difference between both models.

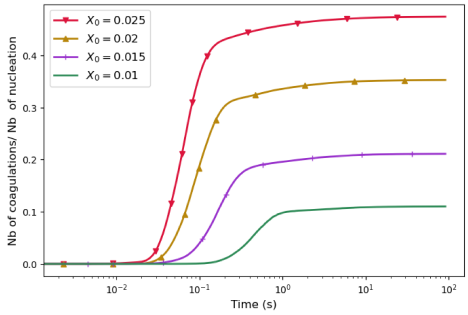

Figure 7: Ratio between the cumulated number of coagulations and the cumulative number of nucleated precipitates for the full-field model.

Moreover, the full-field approach also takes into account precipitates coagulations: when precipitates get close one to another, they coagulate, which also affects the number of precipitates in the system. Fig. 7 shows the ratio between the cumulative number of coagulations and the total number of nucleated precipitates for the different initial concentrations. During the growth stage, all the precipitates grow, increasing their probability of colliding with neighbours, which leads to a surge in the number of coagulations. When the system enters the coarsening stage, the precipitate density decreases and coagulations become less likely, which explains the saturation of the curve in Fig. 7. As expected,

the number of coagulations at the end of the simulation increases with the alloy composition. This figure also shows the high impact of coagulations on the evolution of the microstructure: the ratio almost reaches 50% for $X_0 = 2.5\%$. For such a high coagulation rate, almost every precipitate undergoes a coagulation event.

The consequence of both the nucleation and coagulations effects discussed above can be seen on Fig. 8 that depicts the precipitate density evolution obtained from full-field and mean field models for $X_0 = 1\%$ and $X_0 = 2.5\%$.

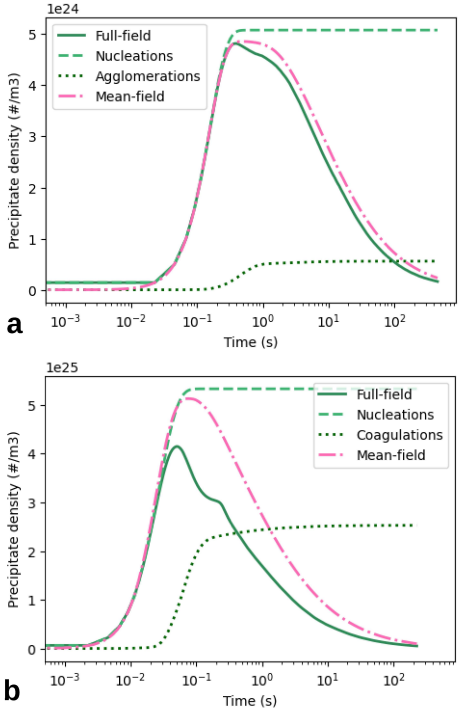

Figure 8: Results for an initial concentration at 1at% (a) and 2.5 at% (b) : comparisons of the total number of precipitates in full-field and mean-field, and number of nucleations and coagulations in full-field.

As shown earlier, the number of nucleation is higher in full-field. However, the precipitate density decreases as soon as coagulation events start occurring. The effect is more pronounced for higher alloy compositions: for $X_0 = 2.5\%$ (see Fig. 8.b), even though the full-field model predicts more nucleation events, the larger number of coagulations leads to a peak precipitate density 20% lower than the prediction of the mean-field model. In addition, because most coagulations occur within a short time window, the time-evolution of the precipitate density is significantly different than predicted by the mean-field approach and shows a characteristic shoulder when the coagulation rate goes down.

4.3. Mean radius evolution and coarsening rate

Coarsening of the precipitate population originates from the Gibbs-Thomson relation that relates the radius of the precipitates to their equilibrium compositions and is permitted by volume diffusion of solutes in the matrix phase. In this situation, scaling arguments [52] can be used to show that the average radius $\bar{R}$ grows as a function of time as:

$$\bar{R}^3(t) = \bar{R}_0^3 + k(t - t_0), \tag{23}$$

where $\bar{R}_0$ denote the radius at arbitrary time t_0 and where k is referred to as the coarsening rate. Lifshitz, Slyozov and Wagner (LSW) were the first to propose an estimate of this coarsening rate [5, 6, 7] valid in the steady state of the coarsening. Adapting the LSW theory to A_xB_y stoichiometric precipitates and to the dilute limit $X_0 \ll 1$ (valid for the Al-Sc system) [53], we obtain:

$$k_{\mathrm{LSW}} = \frac{4}{9}\left(\frac{x+y}{y}\right)^2 D l_0 X_0. \tag{24}$$

where l_0 is the capillary length defined in Eq. (9).

However, in full-field simulations, the coarsening rate can differ from this estimate because (i) the solute interactions between neighbouring precipitates are ignored in the LSW theory, (ii) the system can be far away from the steady-state where Eq. (23) is valid and (iii) the influence of the coagulation events can be non-negligible.

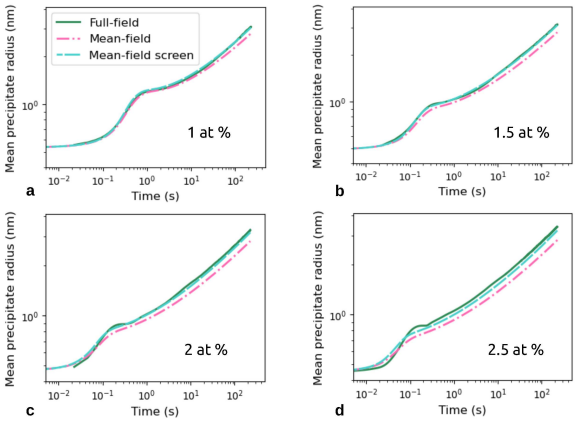

Figure 9: Evolution of the average radius for the full-field model and the mean-field model with and without the screening length accounting for solutal impingement. The full-field results are averaged over five independent simulations.

To investigate these effects, the results of the full-field model are compared with two versions of the mean-field model: its original version that assumes isolated precipitates in a infinite medium (valid for vanishing volume

fraction) and the screened version that accounts for solutal impingement in an average way [8].

Fig. 9 shows the evolution of the mean radius for four initial concentrations and compares the results of the full-field model (green full curve) and the mean-field approaches with and without the screening term (dashed curves). To smooth out the influence of stochastic events appearing in full-field models because of the finite size of the system, the results are averaged from five independent simulations.

In all four cases, the non-screened version of the mean-field model (dashed pink curves) underestimates the coarsening rate compared to the full-field model. In addition, we highlight that incorporating the screening length in the mean-field model leads to a much better agreement with the full-field results. This remarkable agreement can be seen as a validation of the screening theory that captures the influence of solutal impingement. Deviations between both approaches are visible for $X_0 = 2.5$ at.% (Fig. 9) and can be attributed to the role of coagulations that is important at high volume fraction (see Fig. 7) and that is not incorporated into the mean-field approaches. At long times (e.g. $t > 10$ s), the role of coagulations vanishes, which explains why the radius evolution for both the full-field and the mean-field screened are eventually getting closer on Fig. 9.d.

To discuss in more details the differences between the various approaches, the time-dependent coarsening rate is determined by fitting the evolution of the radius, starting at a time t_0 corresponding to the beginning of the coarsening stage and using a sliding time window of duration 50 s.

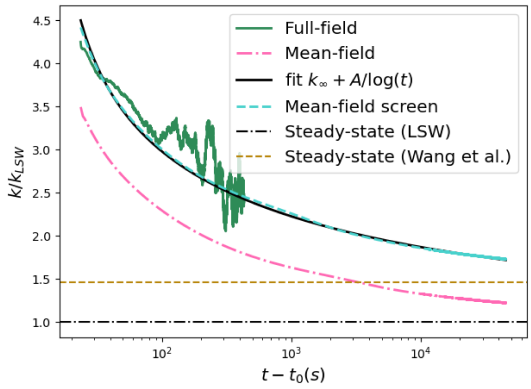

Figure 10: Evolution of the ratio k/k_{LSW} for the different models for $X_0 = 1$ at%. The screened mean-field model is fitted with $k(t) = k_\infty + A/\log(t)$.

Fig. 10 shows the time evolution of the coarsening rate for different models normalized by the value k_{LSW} given in Eq. (24). The black dashed horizontal line therefore represents the prediction of the LSW theory. In addition, the brown dashed line represents the steady-state of the screened mean-field approach predicted by Wang *et al.* [8] and incorporating the screening length.

The oscillations observed for the full-field model are due to the finite number of precipitates in the simulated volume, inducing stochasticity on the estimation of the coarsening rate. These fluctuations become more important at longer times because the number of precipitates decreases with time. Despite these oscillations, the coarsening rate obtained from the full-field model matches the results obtained from the mean-field screened model, reinforcing the agreement between both approaches discussed above. On the other hand, the results obtained with the non-screened version of the mean-field model underestimates significantly the coarsening rate.

Moreover, it can be noted that the results obtained with the full field and the mean field approaches are significantly above the horizontal baselines representing the steady state and appear to converge slowly towards these values. This slow convergence highlights the role of a long transient regime before reaching a steady-state coarsening rate. In particular, the coarsening rate obtained with the screened mean-field model is fitted with $k(t) = k_\infty + A/\log(t)$ (see the thick black line on Fig. 10), revealing that the coarsening rate converges logarithmically towards the steady-state value.

This long transient coarsening stage has been discussed in the literature: in Ref. [54], Chen and Voohrees used a mean-field approach similar the one used here to demonstrate that the coarsening rate converge towards the steady-state prediction at long-times. They also show that the convergence rate strongly depends on the shape of the initial distribution and slow convergence similar to the one discussed here are obtained by starting from modified log-normal distributions. This type of slow convergence has also been shown to be consistent with experimental results [55] and with phase-field simulations [34].

4.4. Evolution of the size distribution

In addition to the evolution of the mean radius during the coarsening phase, the LSW theory also predicts the shape of the particles size distribution in the steady-state coarsening regime [5, 6, 7]. The mathematical description of this steady-state distribution can be found in the literature [5, 6] and it is represented with a continuous black line in Fig. 11(a), (b) and (c).

In contrast with the LSW solution, both the mean-field and full-field models capture the time-dependent

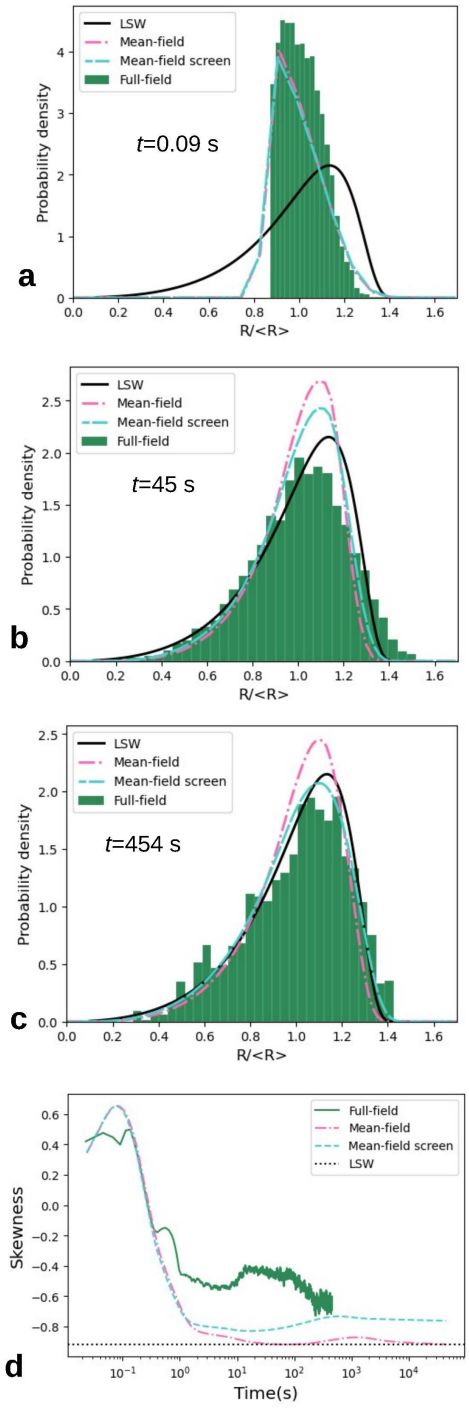

Figure 11: Evolution of the size distribution for a nominal concentration $X_0 = 1$ at.%. (a-c) Size distribution of the precipitate population for the full-field and the mean-field models after a heat treatment of (a) 0.09 s, (b) 45 s and (c) 454 s. (d) time-evolution of the skewness of the size distribution obtained with different models. The full-field results are averaged over five independent simulations.

evolution of the size distribution from the nucleation to the coarsening stages. Fig. 11(a) displays the size distribution obtained for the $X_0 = 1$ at.% alloy at $t = 0.09$ s during the nucleation stage. Both formulations of the mean-field approach yield similar distributions that result from the time evolution of the nucleation rate (Eq. (6)) combined with the growth rate: the larger precipitates have nucleated first with a nucleation rate limited by the incubation time and have undergone the longest growth while the smallest precipitates have nucleated later and are more numerous because of the diminishing effect of the incubation time. It results in a right-skewed distribution typical from the nucleation stage [56, 57]. The distribution obtained from the full-field model follows the same trends because the same expression of the nucleation rate is used; the differences obtained between both approaches at these short time-scales are attributed to the influence of the time-dependent diffusion equation integrated in the full-field model while the growth rate used in the mean-field approach is obtained from the stationary diffusion equation. It seems important to highlight that the distributions obtained at short time-scales with the different models differ significantly from the LSW distribution that is only valid in the steady-state coarsening stage.

Fig. 11(b) compares the size distribution at a intermediate time $t = 45$ s that corresponds to the coarsening stage. Compared to Fig. 11(a), the distributions obtained from the different models have transitioned to left skewed distributions that resemble the LSW function. At this stage, the differences between the mean-field model and the LSW show the influence of the transient coarsening stage on the precipitate distribution evidenced previously [54, 51]. Interestingly, the precipitate distribution obtained with the full-field model appears significantly more symmetric than the mean-field predictions, with a surplus of large precipitate. This can be attributed to the influence of coagulation events that combine two precipitates of average sizes to form a large precipitate.

To compare the distributions obtained after a long coarsening stage, Fig. 11(c) shows precipitates distributions after a time of 454 s. The distribution obtained from the mean-field model (non-screened) converges slowly towards the LSW distribution: the differences between them are attributed to the distance from the steady-state which is a consequence of the long transient regime discussed in section 4.3. On the other hand, the distribution obtained with the screened version of the mean-field model is significantly less peaked, this difference being a consequence of the solutal impingement. This is also supported by the fact that the distri-

bution obtained from the full-field model matches well this latter one. Comparing the full-field distributions shown in Fig. 11(b) and Fig. 11(c) reveals that the effect of coagulation events wears off with time because such events become less likely upon the drop of the precipitate density.

Figs. 11(a), (b) and (c) reveal that the precipitate distribution shifts from a right-skewed distribution characteristic of the nucleation stage to a left-skewed distribution characteristic of the coarsening stage and comparable to the LSW theory. To better characterize the time evolution of the distribution, it is useful to follow the evolution of the skewness γ, a dimensionless coefficient that characterizes the asymmetry of a distribution. It is defined as the third standardized moment and is computed as

$$\gamma = \frac{\mu_3}{\mu_2^{3/2}} \tag{25}$$

where μ_3 and μ_2 are the central moments of order 2 and 3 of the distribution. A positive (respectively negative) skewness translates the fact that the right (resp. left) tail of the distribution is more pronounced. A skewness equal to 0 corresponds to a symmetric distribution.

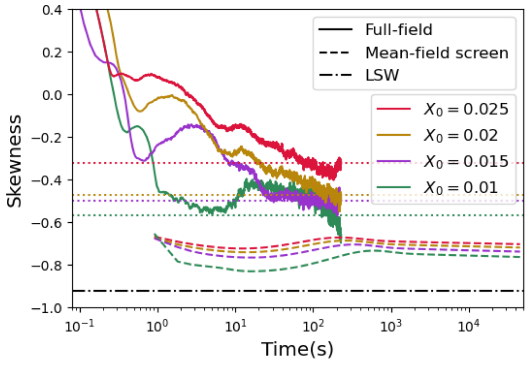

Figure 12: Evolution of the skewness with time for four different initial concentration in solutes. The dotted lines represent the values of the skewness averaged over the last 5000 time-steps ($\sim 2s$) of the full-field simulation. The dash-lines represesent the time-evolution of the skewness obtained from the mean-field screened model.

Fig. 11(c) displays the time evolution of the skewness obtained from the different models. In the first nucleation stage, the distributions exhibit a positive skewness characterizing the distribution shown in Fig. 11(a). Between $t \simeq 0.1$ s and $t \simeq 1$ s, the skewness drops from positive to negative values which translates the transition between the nucleation and growth stages to the coarsening stage.

As expected, the skewness obtained with the mean-field (non screened) model converges to the skewness of the LSW distribution represented with an horizontal dash line. In contrast, the screened mean-field model converges to a higher value, a consequence of the solutal impingement. The skewness obtained with the full-field model follows the same trend as for mean-field approaches. It remains higher during the coarsening stage and eventually drops to a value close to the one obtained with the mean-field screened model. This translates the fact that during the transient coarsening regime, the distributions simulated with the full-field model are significantly more symmetric than the ones obtained from the mean-field approaches, as a consequence of the coagulation events.

The effect of coagulation events on the symmetry of the precipitate density is amplified for higher volume fraction. Fig. 12 compares the time evolution of the skewness for different alloy concentrations. The symmetry of the distribution shape increases with the precipitate volume fraction, significantly more than predicted by the screened mean-field model that only accounts for the role of solutal impingement.

5. Conclusion

We present here a full-field model for precipitation in which the precipitates are described by a shape function with sharp interfaces. This formulation allows for a gain of efficiency compared phase-field models and enables to simulate representative volumes containing a large population of precipitates over long time-scales. The results of the full-field approach are compared to mean-field numerical models to assess the influence of solutal impingement and coagulations of precipitates on the different stages of the nucleation process.

First, we evidenced that more nucleation events occur in the full-field model as compared to the mean-field approach. This is attributed to the spatial description of the concentration fields that take different values while the mean-field approach assumes a single-valued matrix concentration.

This effect is compensated by the influence of coagulations of neighboring precipitates that triggers a drop of the total number of precipitate after their nucleation. As a consequence, the peak number of preciptates is slightly lower in full-field models compared to mean-field approaches. Despite these differences, the evolution of the average radius obtained with full field matches well the prediction of mean-field approaches, especially the screened mean-field model that accounts for solutal impingement in an average way.

Our results also highlight the influence of the long transient regime that approaches asymptotically the

steady-state predictions [8, 54]. During this transient regime, the coarsening rate is significantly higher than its steady-state value and the precipitate distribution is significantly more symmetric. The comparison between full field and mean field results also put in evidence the role of coagulation events on the precipitate distribution: coagulations lead to the formation of larger precipitates and thereby symmetrize the size distribution. Because the number of coagulations drops during the coarsening stage, their influence slowly wears off along the coarsening stage.

Size distributions observed experimentally in metallic alloys can deviate significantly from the LSW size distribution. In particular, a number of previous studies evidenced symmetric distributions or right-skewed log-normal distributions of precipitate sizes [58, 59, 21, 60, 61]. The present work shows that these differences can be attributed to multiple effects:

- the role of solutal impingement increases with the volume fraction of precipitate and leads to more symmetric steady-state distributions [8].
- the influence of the long transient coarsening regime and the slow convergence of the precipitate distribution to a steady-state LSW-like distribution, as evidenced previously [54, 59].
- the influence of precipitate coagulations that lead to a higher number of large precipitates and symmetries the size distribution.

At this point, we also have to discuss some drawbacks of the current implementation of the full-field model. In this study, there is no limitation to the coagulation of precipitates, while in Al-Sc alloys, the coagulation of ordered Al_3Sc preciptates is limited by the existence of four translational variants [25] that prevents the coagulation of precipitates with different variants. Such effect can be included in the present full-field model by attributing a variant (1, 2, 3 or 4) at random to precipitates and allowing the coagulation of neighboring precipitates only if their variants are identical. Preliminary results including this effect reveals that the number of agglomerations is significantly reduced, but the general trends discussed throughout the paper remain valid.

In addition, coherent precipitates in metallic alloys also interact through elastic fields [25], which can modify their evolution [62, 63]. It would be desirable to extend the current full-field model to account for these effects. This could be done by computing the elastic energy of a population of precipitates and by adjusting the position of the precipitates to minimize this energy.

Furthermore, the results presented here focus on spherical precipitates while a majority of technologically relevant systems (in particular Al and Ni-based alloys) display non-spherical precipitates [1, 2]. We note that it is straightforward to extent the present model to non-spherical precipitates by using different shape functions, and by adjusting the Gibbs-Thomson effect to these new geometries [64, 65].

Also, this article focuses on homogeneous isothermal thermal treatments but it would be straightforward to use the full-field model to investigate the influence of a complex heterogeneous thermal history encountered during processes such as additive manufacturing and welding. The full-field model could be used to assess the domain of validity of mean-field approaches for complex thermal treatment that involve sharp thermal gradients and high heating/cooling rates.

One of the advantage of this meso-scale full-field model is that it generates representative microstructures obtained from nucleation, growth and coarsening stages, and encodes the spatial correlations between precipitates resulting from these stages. A natural prospect of this work therefore consists in using these microstructures in dislocation dynamics numerical approaches [66, 67] to model the dislocations/precipitates interactions in order to predict the yield stress of the alloy and discuss more carefully the assumptions of the mean-field approach commonly used the relate the mechanical properties of the alloy to the precipitate microstructure [1, 68, 69].

Acknowledgement

The financial support of INSA-Lyon through a doctoral scholarship on societal issues is gratefully acknowledged. Also, we would like to acknowledge the support of NVIDIA Corporation with the donation of a Titan V GPU used for this research.

References

[1] C. Sigli, F. De Geuser, A. Deschamps, J. Lépinoux, M. Perez, Recent advances in the metallurgy of aluminum alloys. Part II: Age hardening, Comptes Rendus Physique 19 (8) (2018) 688–709.

[2] A. Deschamps, C. Hutchinson, Precipitation kinetics in metallic alloys: Experiments and modeling, Acta Materialia 220 (2021) 117338.

[3] A. Ardell, Precipitation hardening, Metallurgical Transactions A 16 (1985) 2131–2165.

[4] E. Nembach, Particle strengthening of metals and alloys, Wiley, 1997.

[5] I. Lifshitz, V. Slyozov, The kinetics of precipitation from supersaturated solid solutions, Journal of physics and chemistry of solids 19 (1-2) (1961) 35–50.

[6] C. Wagner, Theorie der Alterung von Niederschlägen durch Umlösen (Ostwald-Reifung), Zeitschrift für Elektrochemie, Berichte der Bunsengesellschaft für physikalische Chemie 65 (7-8) (1961) 581–591.

[7] A. Baldan, Review progress in Ostwald ripening theories and their applications to nickel-base superalloys Part I: Ostwald ripening theories, Journal of materials science 37 (2002) 2171–2202.

[8] K. Wang, M. Glicksman, K. Rajan, Length scales in phase coarsening: Theory, simulation, and experiment, Computational materials science 34 (3) (2005) 235–253.

[9] B. Pletcher, K. Wang, M. Glicksman, Experimental, computational and theoretical studies of δ' phase coarsening in Al–Li alloys, Acta Materialia 60 (16) (2012) 5803–5817.

[10] R. Wagner, R. Kampmann, P. Voorhees, Homogeneous second-phase precipitation, Phase transformations in materials (2001) 309–407.

[11] M. Perez, M. Dumont, D. Acevedo-Reyes, Implementation of classical nucleation and growth theories for precipitation, Acta Materialia 56 (9) (2008) 2119–2132. doi:https://doi.org/10.1016/j.actamat.2007.12.050.

[12] N. Ury, R. Neuberger, N. Sargent, W. Xiong, R. Arróyave, R. Otis, Kawin: An open source Kampmann–Wagner Numerical (KWN) phase precipitation and coarsening model, Acta Materialia 255 (2023) 118988. doi:10.1016/j.actamat.2023.118988.

[13] E. Kozeschnik, MatCalc - A simulation tool for multicomponent thermodynamics, diffusion and phase transformations, Mathematical Modelling of Weld Phenomena 5 349.

[14] E. Kozeschnik, J. Svoboda, P. Fratzl, F. D. Fisher, Modelling of kinetics in multi-component multi-phase systems with spherical precipitates II: Numerical solution and application, Materials Science and Engineering: A A385 (2004) 157–165.

[15] J. Svoboda, F. D. Fisher, P. Fratzl, E. Kozeschnik, Modelling of kinetics in multi-component multi-phase systems with spherical precipitates I: Theory, Materials Science and Engineering: A A385 (2004) 166–174.

[16] Q. Chen, K. Wu, G. Sterner, P. Mason, Modeling Precipitation Kinetics During Heat Treatment with Calphad-Based Tools, Journal of Materials Engineering and Performance 23 (12) (2014) 4193–4196. doi:10.1007/s11665-014-1255-6.

[17] D. Bardel, M. Perez, D. Nelias, A. Deschamps, C. Hutchinson, D. Maisonnette, T. Chaise, J. Garnier, F. Bourlier, Coupled precipitation and yield strength modelling for non-isothermal treatments of a 6061 aluminium alloy, Acta Materialia 62 (2014) 129–140.

[18] D. Bardel, M. Fontaine, T. Chaise, M. Perez, D. Nelias, F. Bourlier, J. Garnier, Integrated modelling of a 6061-T6 weld joint: From microstructure to mechanical properties, Acta Materialia 117 (2016) 81–90. doi:10.1016/j.actamat.2016.06.017.

[19] A. Balan, M. Perez, T. Chaise, S. Cazottes, D. Bardel, F. Corpace, F. Pichot, A. Deschamps, F. De Geuser, D. Nelias, Precipitation of γ'' in inconel 718 alloy from microstructure to mechanical properties, Materialia 20 (2021) 101187.

[20] M. Anderson, C. Panwisawas, Y. Sovani, R. Turner, J. Brooks, H. Basoalto, Mean-field modelling of the intermetallic precipitate phases during heat treatment and additive manufacture of Inconel 718, Acta Materialia 156 (2018) 432–445.

[21] M. Anderson, F. Schulz, Y. Lu, H. Kitaguchi, P. Bowen, C. Argyrakis, H. Basoalto, On the modelling of precipitation kinetics in a turbine disc nickel based superalloy, Acta Materialia 191 (2020) 81–100.

[22] Y. Li, Z. Wang, X. Gao, Y. Wang, J. Li, J. Wang, Revisiting transient coarsening kinetics: a new framework in the Lifshitz-Slyozov-Wagner space, Acta Materialia 237 (2022) 118196.

[23] P. Voorhees, M. Glicksman, Solution to the multi-particle diffusion problem with applications to Ostwald ripening — II. Computer simulations, Acta Metallurgica 32 (11) (1984) 2013–2030.

[24] L. Chen, Phase-field models for microstructure evolution, Annual review of materials research 32 (1) (2002) 113–140.

[25] A. Finel, Y. Le Bouar, A. Gaubert, U. Salman, Phase field methods: microstructures, mechanical properties and complexity, Comptes Rendus Physique 11 (3-4) (2010) 245–256.

[26] Y. Ji, A. Issa, T. Heo, J. Saal, C. Wolverton, L. Chen, Predicting β' precipitate morphology and evolution in Mg-Re alloys using a combination of first-principles calculations and phase-field modeling, Acta materialia 76 (2014) 259–271.

[27] K. Kim, A. Roy, M. Gururajan, C. Wolverton, P. Voorhees, First-principles/phase-field modeling of θ' precipitation in Al-Cu alloys, Acta Materialia 140 (2017) 344–354.

[28] S. Hu, L. Chen, A phase-field model for evolving microstructures with strong elastic inhomogeneity, Acta Materialia 49 (11) (2001) 1879–1890.

[29] G. Boussinot, A. Finel, Y. Le Bouar, Phase-field modeling of bimodal microstructures in nickel-based superalloys, Acta Materialia 57 (3) (2009) 921–931.

[30] C. Yenusah, Y. Ji, Y. Liu, T. Stone, M. Horstemeyer, L. Chen, L. Chen, Three-dimensional phase-field simulation of γ'' precipitation kinetics in Inconel 625 during heat treatment, Computational Materials Science 187 (2021) 110123.

[31] D. Fan, S. Chen, L. Chen, P. Voorhees, Phase-field simulation of 2-D Ostwald ripening in the high volume fraction regime, Acta Materialia 50 (8) (2002) 1895–1907.

[32] D. Molnar, R. Mukherjee, A. Choudhury, A. Mora, P. Binkele, M. Selzer, B. Nestler, S. Schmauder, Multiscale simulations on the coarsening of Cu-rich precipitates in α-Fe using kinetic Monte Carlo, molecular dynamics and phase-field simulations, Acta Materialia 60 (20) (2012) 6961–6971.

[33] S. Kim, Large-scale three-dimensional simulation of ostwald ripening, Acta Materialia 55 (19) (2007) 6513–6525.

[34] J. Li, C. Guo, Y. Ma, Z. Wang, J. Wang, Effect of initial particle size distribution on the dynamics of transient Ostwald ripening: A phase field study, Acta Materialia 90 (2015) 10–26.

[35] A. Finel, Y. Le Bouar, B. Dabas, B. Appolaire, Y. Yamada, T. Mohri, Sharp phase field method, Physical Review Letters 121 (2) (2018) 025501.

[36] D. Tourret, A. Karma, Multiscale dendritic needle network model of alloy solidification, Acta Materialia 61 (17) (2013) 6474–6491.

[37] D. Tourret, A. Karma, Three-dimensional dendritic needle network model for alloy solidification, Acta Materialia 120 (2016) 240–254.

[38] P. Geslin, C. Chen, A. Tabrizi, A. Karma, Dendritic needle network modeling of the Columnar-to-Equiaxed transition. Part I: two dimensional formulation and comparison with theory, Acta Materialia 202 (2021) 42–54.

[39] C. Chen, A. Tabrizi, P. Geslin, A. Karma, Dendritic needle network modeling of the Columnar-to-Equiaxed Transition. Part II: three dimensional formulation, implementation and comparison with experiments, Acta Materialia 202 (2021) 463–477.

[40] D. Tourret, M. Francois, A. Clarke, Multiscale dendritic needle network model of alloy solidification with fluid flow, Computational Materials Science 162 (2019) 206–227.

[41] T. Isensee, D. Tourret, Convective effects on columnar dendritic solidification–A multiscale dendritic needle network study, Acta Materialia 234 (2022) 118035.

[42] E. Marquis, D. Seidman, Nanoscale structural evolution of Al_3Sc precipitates in Al(Sc) alloys, Acta Materialia 49 (11) (2001) 1909–1919.

[43] D. Seidman, E. Marquis, D. Dunand, Precipitation strengthening at ambient and elevated temperatures of heat-treatable

Al(Sc) alloys, Acta Materialia 50 (16) (2002) 4021–4035.
[44] S. Iwamura, Y. Miura, Loss in coherency and coarsening behavior of Al_3Sc precipitates, Acta Materialia 52 (3) (2004) 591–600.
[45] E. Kozeschnik, Modeling Solid-State Precipitation, Computational Materials Science and Engineering, Momentum Press, 2013.
[46] P. Maugis, F. Soisson, L. Laé, Kinetics of precipitation: Comparison between Monte Carlo simulations, cluster dynamics and the classical laws, in: Defect and diffusion Forum, Vol. 237, Trans Tech Publ, 2005, pp. 671–676.
[47] M. P., Gibbs–Thomson effects in phase transformations, Scripta Materialia 52 (8) (2005) 709–712. doi:https://doi.org/10.1016/j.scriptamat.2004.12.026.
[48] J. Simmons, C. Shen, Y. Wang, Phase field modeling of simultaneous nucleation and growth by explicitly incorporating nucleation events, Scripta Materialia 43 (10) (2000) 935–942.
[49] Thermo-Calc Software TCAL4 and MOBAL3 Aluminum-based Alloys Database, `https://thermocalc.com/products/databases/aluminum-based-alloys/`.
[50] C. Zener, Theory of growth of spherical precipitates from solid solution, Journal of Applied Physics 20 (10) (1949) 950–953.
[51] Q. Wang, H. Xiong, A high-resolution population dynamic model for predicting homogeneous precipitation kinetics of spherical precipitates during thermal aging, Metallurgical and Materials Transactions A 52 (2021) 4987–4996.
[52] C. Herring, Effect of change of scale on sintering phenomena, Journal of Applied Physics 21 (4) (1950) 301–303.
[53] H. Calderon, P. Voorhees, J. Murray, G. Kostorz, Ostwald ripening in concentrated alloys, Acta metallurgica et materialia 42 (3) (1994) 991–1000.
[54] M. Chen, P. Voorhees, The dynamics of transient Ostwald ripening, Modelling and Simulation in Materials Science and Engineering 1 (5) (1993) 591.
[55] V. Snyder, J. Alkemper, P. Voorhees, Transient Ostwald ripening and the disagreement between steady-state coarsening theory and experiment, Acta Materialia 49 (4) (2001) 699–709.
[56] E. Clouet, M. Nastar, A. Barbu, C. Sigli, G. Martin, Precipitation in Al-Zr-Sc alloys: A comparison between kinetic Monte Carlo, cluster dynamics and classical nucleation theory, arXiv preprint cond-mat/0507259.
[57] E. Clouet, A. Barbu, L. Laé, G. Martin, Precipitation kinetics of Al_3Zr and Al_3Sc in aluminum alloys modeled with cluster dynamics, Acta Materialia 53 (8) (2005) 2313–2325.
[58] T. Hirata, D. Kirkwood, The prediction and measurement of precipitate number densities in a nickel-6.05 wt.% aluminium alloy, Acta Metallurgica 25 (12) (1977) 1425–1434.
[59] K. Vedula, R. Heckel, Spheroidization of binary Fe-C alloys over a range of temperatures, Metallurgical Transactions 1 (1970) 9–18.
[60] D. Acevedo-Reyes, M. Perez, C. Verdu, A. Bogner, T. Epicier, Characterization of precipitates size distribution: validation of low-voltage STEM, Journal of Microscopy 232 (1) (2008) 112–122.
[61] Z. Hou, R. Babu, P. Hedström, J. Odqvist, On coarsening of cementite during tempering of martensitic steels, Materials Science and Technology 36 (7) (2020) 887–893.
[62] J. Zhu, T. Wang, A. Ardell, S. Zhou, Z. Liu, L. Chen, Three-dimensional phase-field simulations of coarsening kinetics of γ' particles in binary Ni–Al alloys, Acta Materialia 52 (9) (2004) 2837–2845.
[63] M. Cottura, Y. Le Bouar, B. Appolaire, A. Finel, Role of elastic inhomogeneity in the development of cuboidal microstructures in Ni-based superalloys, Acta Materialia 94 (2015) 15–25.
[64] B. Holmedal, E. Osmundsen, Q. Du, Precipitation of non-spherical particles in aluminum alloys part I: generalization of the Kampmann–Wagner numerical model, Metallurgical and Materials Transactions A 47 (2016) 581–588.
[65] Y. Li, B. Holmedal, H. Li, L. Zhuang, J. Zhang, Q. Du, Precipitation and strengthening modeling for disk-shaped particles in aluminum alloys: size distribution considered, Materialia 4 (2018) 431–443.
[66] B. Devincre, R. Madec, G. Monnet, S. Queyreau, R. Gatti, L. Kubin, Modeling crystal plasticity with dislocation dynamics simulations: The "microMegas" code, Mechanics of Nano-objects 1 (2011) 81–100.
[67] A. Arsenlis, W. Cai, M. Tang, M. Rhee, T. Oppelstrup, G. Hommes, T. Pierce, V. Bulatov, Enabling strain hardening simulations with dislocation dynamics, Modelling and Simulation in Materials Science and Engineering 15 (6) (2007) 553.
[68] J. Friedel, Dislocations, International Series of Monographs on Solid State Physics, Pergamon Press, 1964.
[69] A. Argon, Strengthening mechanisms in crystal plasticity, Vol. 4 of Oxford series on materials modelling, OUP Oxford, 2008.
[70] R. Kampmann, R. Wagner, Kinetics of precipitation in metastable binary alloys-theory and application to Cu-1.9 at% Ti and Ni-14 at% Al, Decomposition of alloys: the early stages (1984) 91–103.
[71] O. Myhr, Ø. Grong, Modelling of non-isothermal transformations in alloys containing a particle distribution, Acta Materialia 48 (7) (2000) 1605–1615.
[72] D. Zhao, Y. Xu, S. Gouttebroze, J. Friis, Y. Li, Modelling the age-hardening precipitation by a revised langer and schwartz approach with log-normal size distribution, Metallurgical and Materials Transactions A 51 (2020) 4838–4852.
[73] M. Bignon, P. Shanthraj, J. Robson, Modelling dynamic precipitation in pre-aged aluminium alloys under warm forming conditions, Acta Materialia 234 (2022) 118036.
[74] P. Valdenaire, Plasticité cristalline: Equations de transport et densités de dislocations, Ph.D. thesis, Paris Sciences et Lettres (2016).

Appendix A. Numerical integration of the mean-field model

In order to understand how the full-field character of the model influences the results, we compare it with a mean-field approach for precipitation. This type of model was first introduced by Kampmann and Wagner [70] and have been largely used for precipitation kinetics modeling [2, 10, 11, 51, 71, 72, 73]. In these approaches, the precipitate microstructure is represented by a size distribution discretized in a finite number "classes" that evolve according to the nucleation, growth and shrinkage of precipitates.

This type of models can be divided into two categories depending on the treatment of the size distribution: in the Lagrangian-type models [11, 2], a "class" gathers precipitates that nucleated at the same time and the radius of each class evolves in time from the integration of the growth equation. In contrast, in the Eulerian-type approaches [10, 51, 71, 72], the size distribution is dicretized in classes of finite width such that precipitates

change classes along the simulations. Both methods offer advantages discussed in Ref. [11], and we opted for the latter case because of its natural connection with the size distribution employed in the LSW theory. In particular, the mean-field model employed here and its numerical implementation are similar with the ones described in Ref. [51] and are briefly recalled in the following.

We note $f(R)$ the precipitate size distribution per unit volume.

The nominal alloy composition X_0 is distributed between precipitates and matrix, such that the atomic fraction in the matrix is given by:

$$X_m = \frac{X_0 - X_p \phi_p \frac{v_{at}^m}{v_{at}^p}}{1-\phi}, \tag{A.1}$$

where

$$\phi_p = \frac{4\pi}{3} \int_0^{+\infty} f(R,t) R^3 dR \tag{A.2}$$

is the volume fraction of precipitates.

Considering that the radius of each precipitates evolves smoothly in time, the size distribution $f(R)$ is subjected to the following continuity equation:

$$\frac{\partial f(R,t)}{\partial t} + \frac{\partial}{\partial R}\left(v(R,t) f(R,t)\right) = \frac{dN}{dt}\delta(R - R_{kT}^*) \tag{A.3}$$

where $\frac{dN}{dt}$ is the nucleation rate at time t and R_{kT}^* is the critical nucleation radius. For the sake of consistency with the full-field model described in this work, we consider that $\frac{dN}{dt}$ is given by Eq. (6) taken for $X = X_m$ and that the nucleation radius is given by Eq. (7).

The growth rate of the precipitates is obtain from resolving the stationary diffusion equation around an isolated precipitate and computing the flux of solutes towards the precipitate. We thus obtain:

$$v(R,t) = \frac{D}{R} \frac{X_m(t) - X_R}{\left(\frac{v_m^{at}}{v_p^{at}} X_p - X_R\right)}. \tag{A.4}$$

where X_R is the equilibrium composition at the precipitate/matrix interface given by Gibbs-Thomson relation Eq. (8). To avoid numerical instabilities related to the divergence of this the Gibbs-Thomson equation for small radii, we limit X_R by a maximum value $X_{max} = \frac{1}{2}\left(X_m + \frac{v_m^{at}}{v_p^{at}} X_p\right)$. This quantity is chosen based on the characteristic time R^2/D to dissolve a precipitate or radius R. Overall, the equilibrium composition at the precipitate/matrix interface is given by:

$$X_R = \min\left(\frac{1}{2}\left(X_m + \frac{v_m^{at}}{v_p^{at}} X_p\right), X_{eq} \exp\left(\frac{x+y}{y}\frac{l_0}{R}\right)\right). \tag{A.5}$$

The growth and coarsening of precipitates naturally arises from the time integration of Eqs. (A.4) and (A.5).

Implementing numerically the model requires to discretize the distribution $f(R,t)$ in a finite number of classes of size ΔR while the time is discretized in steps Δt.

The nucleation term of Eq. (A.3) is simply incorporated by adding $\frac{dN}{dt}\Delta t$ precipitates of size R_{kT}^* at each time steps. This quantity is distributed pro rata between classes of radii R_n and R_{n+1} ($R_n < R^* < R_{n+1}$). For clarity reasons, this source term is not accounted for in the following equations that detail the numerical scheme.

After discretization of Eq. (A.3) with finite differences, we obtain:

$$f_i^{t+\Delta t} = f_i^t - \frac{\Delta t}{\Delta R}\left[F_{i+\frac{1}{2}}^t - F_{i-\frac{1}{2}}^t\right] \tag{A.6}$$

where $F_{i+1/2}^t$ denote the fluxes of precipitates between classes of radius R_i and R_{i+1}.

Several choices can be made for the expression of $F_{i+1/2}^t$. A simple solution is to use a classical upwind scheme [11, 71] that remains numerically stable for sharply varying distribution as obtained in the first nucleation stage. However, the simple upwind scheme is impaired by spurious numerical diffusion terms [74] and does not allow to integrate precisely the transport equation Eq. (A.3) for smooth size distribution encountered at the later coarsening stage. Following Ref. [51], the upwind scheme is corrected with an anti-diffusion term of the form:

$$F_{i+\frac{1}{2}} = F_{i+\frac{1}{2}}^{\text{up}} + \frac{1}{2} v_{i+\frac{1}{2}}\left(1 - \frac{\Delta t}{\Delta R}|v_{i+\frac{1}{2}}|\right)(f_{i+1} - f_i)\Phi_{i+\frac{1}{2}}, \tag{A.7}$$

where

$$v_{i+\frac{1}{2}} = \frac{1}{2}\left(v_i + v_{i+1}\right), \tag{A.8}$$

and

$$F_{i+\frac{1}{2}}^{\text{up}} = \begin{cases} f_i v_{i+\frac{1}{2}}, & \text{if } v_{i+\frac{1}{2}} > 0 \\ f_{i+1} v_{i+\frac{1}{2}}, & \text{if } v_{i+\frac{1}{2}} \leq 0. \end{cases} \tag{A.9}$$

The term $\Phi_{i+1/2}$ is a flux limiter that must converge to 0 (respectively 1) for sharply (resp. smoothly) varying distributions. To quantify this character, we introduce a smoothness parameter defined as

$$\theta_{i+\frac{1}{2}} = \begin{cases} \frac{f_i - f_{i-1}}{f_{i+1} - f_i}, & \text{if} f_{i+1} \neq f_i \\ 1, & \text{otherwise.} \end{cases} \tag{A.10}$$

Several choices are possible to relate the flux-limiter $\Phi_{i+1/2}$ to the smoothness parameter $\theta_{i+1/2}$, and different flux-limiter functions have been shown to be suited to different problem. In particular, trial and error have demonstrated that an appropriate flux-limited function for our case is:

$$\Phi(\theta) = \min\left(2\theta, 2\sqrt{\frac{\theta}{\theta+3}}\right). \tag{A.11}$$

With this choice, the precipitate size distribution converges to the expected LSW distribution for long coarsening times.

In practice, the numerical integration of the mean-field model consists in iterating the following steps :

1. The matrix composition is computed using Eq. (A.1) with $\phi_p = \frac{4}{3}\pi \sum_i f_i R_i^3$.
2. The nucleation rate is computed with Eq. (6) and precipitates of radius R^* are added in the appropriate classes.
3. The growth rates v_i corresponding to each class are computed with Eq. (A.3).
4. The fluxes between classes are computed using Eq. (A.7).
5. The time-evolution of the precipitate density is integrated with Eq. (A.6).

The mean-field formulation described above considers that each precipitate is isolated and uses the diffusion field in an infinite matrix to obtain the growth-rate of Eq. (A.4). It does not account for solutal impingement emerging from neighbouring precipitates and is therefore only valid in the limit of vanishing precipitate volume fraction.

To overcome this limitation, Wang et al. suggested to incorporate the role of solutal impingement in an effective screening length R_0 on the solute field. This treatment is well adapted to this mean-field approach, as it only consists in multiplying the growth-rate of Eq. (A.4) by a prefactor that increases with the precipitate volume fraction. Following Ref. [8], the growth rate becomes:

$$v(R,t) = \frac{D}{R}\frac{X_m(t) - X_R}{\left(\frac{v_m^{at}}{v_p^{at}}X_p - X_R\right)}\left(1 + \frac{R}{R_0}\right) \tag{A.12}$$

$$\text{with } R_0 = \sqrt{\frac{\langle R^3\rangle}{3\langle R\rangle\phi_p}}$$

For vanishing precipitate volume fractions $\phi_p \to 0$, R_0 diverges and we recover Eq. (A.4). This version of the mean-field model is refered to as "screened" in the main text of this article.

Appendix B. Choice of the grid spacing

The advantage of the sharp-interface full-field model presented in this paper is that the grid-spacing Δx used for the diffusion equation can be chosen independently from the capillary length as the Gibbs-Thomson relation is used to impose the precipitate concentration that serves as a boundary condition to the diffusion problem. However, the choice of the grid spacing also influences the imprint of the precipitates on the discrete grid and the surrounding diffusion field.

To assess the influence of the grid spacing on the results, simulations for the growth of isolated precipitates have been performed for different grid spacing. We employ the same conditions as in section 3 and use an initial matrix concentration $X_0 = 1$ at%. The time-evolution of the precipitate radius is depicted in Fig. B.13. To highlight the differences between the various cases, we only show the first stages of the growth process; the influence of the grid-spacing tend to dissipate at longer time where $R \gg \Delta x$.

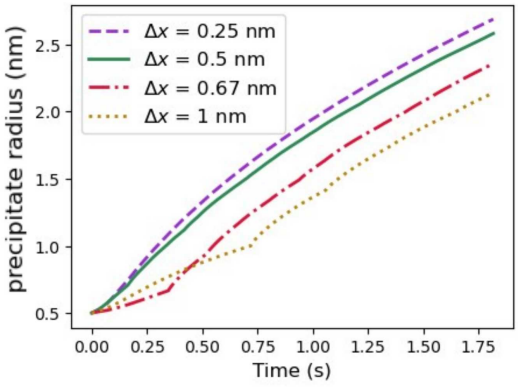

Figure B.13: Evolution of the precipiate radius for different grid spacings for a precipitate growing in a supersaturated matrix of composition $X_0 = 1$ at%.

Fig. B.13 reveals that the choice of Δx influences the first stages of the precipitate growth. In particular, the precipitate radius evolution obtained for $\Delta x = 0.67$ nm and $\Delta x = 1$ nm is significantly different from the results obtained for $\Delta x = 0.25$ nm and $\Delta x = 0.5$ nm, and display a distinctive slope discontinuity at $R = \Delta x$. Below this threshold, the precipitate occupies a unique voxel, and the solute field in its vicinity is not representative of the diffusion field around a spherical object. This leads to an underestimation of the solutal flux and of the growth rate. However, it is worthy to note that the results obtained for $\Delta x = 0.25$ nm and $\Delta x = 0.5$ nm are very close to one another, revealing that discetizing with

$\Delta x = 0.5$ nm is fine enough to reproduce the appropriate growth rate.

In simulations discussed in section 4 that incorporate nucleation, growth and coarsening during a precipitation treatment, the precipitate largely satisfy the condition $R > \Delta x = 0.5$ nm. Indeed, the nucleation radius R^*_{kT} vary between 0.36 nm et 0.48 nm depending on the concentration of the alloy and the nucleated precipitates quickly grow passed $R = \Delta x$. In addition, when the precipitates shrink, they are removed from the simulation if their radius goes below $R_{th} \simeq 0.3$ nm (given by Eq. (15)). As shown in Fig. 4.d, the shrinking dynamics is fast, such that the vast majority of precipitates satisfy $R > \Delta x$ during the simulations discussed in section 4.